Advanced Functional Materials

ADVANCED FUNCTIONAL MATERIALS
www.afm-journal.de

RESEARCH ARTICLE

Multi-Self-Trapped-Exciton Engineering in Sb-Doped Zr-Hybrid-Halides Towards Near-Unity Quantum Efficiency and Excitation-Tunable Luminescence

Luyao Wei[1] | Shilin Jin[1] | Wanxin Shi[2] | Zhenghuan Lin[2] | Yuehua Chen[1] | Lingwei Zeng[3] | Daqin Chen[1,4]

[1]College of Physics and Energy, Fujian Normal University, Fuzhou, China | [2]Fujian Key Laboratory of Polymer Materials, College of Chemistry and Materials Science, Fujian Normal University, Fuzhou, China | [3]School of Chemistry and Chemical Engineering, Key Laboratory of Theoretical Organic Chemistry and Functional Molecule of Ministry of Education, Hunan University of Science and Technology, Xiangtan, Hunan, China | [4]Fujian Provincial Engineering Technology Research Center of Solar Energy Conversion and Energy Storage, Fuzhou, China

Correspondence: Daqin Chen (dqchen@fjnu.edu.cn)

Received: 6 January 2026 | **Revised:** 9 May 2026 | **Accepted:** 13 May 2026

Keywords: hybrid metal halides | phosphorescence | self-trapped exciton | tunable luminescence

ABSTRACT

Luminescent materials with simultaneously high quantum efficiency and excitation-tunable emission are highly desirable for advanced optoelectronic and information-security applications, yet remain challenging to realize within a single, lead-free material system. Here, we report a multi-self-trapped-exciton (STE) engineering strategy in Zr-based hybrid halides, where the deliberate introduction of Sb^{3+} ions reconstructs the excitonic energy landscape of a zero-dimensional host. Beyond the intrinsic Zr-centered STE emission, Sb doping activates multiple Sb-related STE states that efficiently capture organic triplet excitons, effectively suppressing room-temperature phosphorescence while dramatically enhancing radiative recombination. As a result, the obtained phosphors simultaneously achieve nearly perfect photoluminescence efficiency and pronounced excitation-dependent luminescence, with emission color continuously tunable from warm white to orange-red. A 4×8 dot matrix system for ASCII encoding was designed using these materials, demonstrating a dynamic, time-sequential decoding process that enhances information concealment and encryption. Finally, the materials were also incorporated into a digital display model for optical information encryption, where a deceptive message transforms into true information under different excitation wavelengths. This work emphasizes the attractiveness of Sb: $ETPP_2ZrCl_6$ materials for high-security applications, offering a new approach for developing advanced optoelectronic devices and smart labels.

1 | Introduction

All-inorganic lead halide perovskites have emerged as a new class of semiconductor emitters and have attracted intense interest from both academia and industry over the past decade owing to their outstanding optoelectronic properties [1–5], including large absorption coefficients, tunable band gaps, high color purity, high carrier mobilities, and high photoluminescence quantum yields (PLQY). However, the toxicity of lead and the intrinsic instability of lead halide perovskites severely hinder their commercial deployment. To address these issues, extensive efforts have been devoted to substituting Pb^{2+} following design principles that consider ionic radii, charge balance, chemical reactivity, and structural tolerance factors. Group-14 cations Sn^{2+} and Ge^{2+} [6–9], which share a similar ns^2 electronic configuration with Pb^{2+}, are often regarded as ideal substitutes because their incorporation

Luyao Wei and Shilin Jin contributed equally to this work.

can preserve the typical three-dimensional perovskite framework while maintaining favorable optical properties. Nevertheless, the relatively high energy of their ns orbitals makes Sn^{2+} and Ge^{2+} highly susceptible to oxidation into Sn^{4+} and Ge^{4+} in air, thereby destroying the ns^2 configuration and causing pronounced performance degradation, which greatly limits their application in optoelectronic devices.

Currently, heterovalent substitution at the B-site to construct eco-friendly and structurally stable lead-free double perovskites have emerged as an attractive alternative strategy. For example, introducing one tetravalent cation (e.g., Sn^{4+}, Zr^{4+}, Hf^{4+}) together with one vacancy to replace two Pb^{2+} ions can yield zero-dimensional (0D) vacancy-ordered lead-free double perovskites [10–14]. Representative compounds in this family include Cs_2ZrCl_6, Cs_2SnCl_6, and Cs_2HfCl_6. However, because half of the octahedral B sites are occupied by vacancies, these vacancy-ordered structures are prone to octahedral tilting and rotation during phase transitions, which lowers the crystal symmetry and results in optoelectronic performances that still fall short of their lead-based counterparts. On the other hand, the intrinsically reduced structural dimensionality of double perovskites often favors the formation of self-trapped excitons (STEs), which play a pivotal role in governing and enhancing their optical properties [15–17]. For instance, Cs_2HfCl_6 microcrystals synthesized via a solution method exhibit broadband blue emission arising from STE states associated with the distortion of $[HfCl_6]^{2-}$ octahedra [15].

As an alternative, organic-inorganic hybrid metal halides have garnered tremendous interest owing to their rich optoelectronic properties and compatibility with low-cost solution processing [18–20]. Compared with all-inorganic perovskites, hybrid halides integrate the advantages of organic components and inorganic metal halide frameworks, thereby offering a broader compositional and structural space for rational design. On the one hand, organic species can participate in host-guest assembly to construct more rigid crystal lattices, effectively suppressing nonradiative relaxation processes [21, 22]. On the other hand, organic cations can act as independent emissive centers, imparting richer photophysical behaviors and highly tunable emission characteristics to the materials [23–25]. For example, Quan et al. developed a family of $(Ph_3S)_2Sn_{1-x}Te_xCl_6$ (Ph_3S = triphenylsulfonium) compounds, in which the competition between the excited states of organic and inorganic units enables cooperative regulation of afterglow and STE emission [22]. Xia et al. reported the $ATPP_2SnCl_6$: Sb^{3+} (ATPP = acetonyltriphenylphosphonium) system that exploits multiple emissive centers to realize high-order information encryption [26]. These advances position organic-inorganic hybrid perovskites as a new generation of optoelectronic materials and promising lead-free alternatives to conventional lead halide perovskites in diverse optoelectronic and photovoltaic applications.

Recently, Zhou et al. constructed the 0D hybrid $ETPP_2ZrCl_6$ ($ETPP^+$ = ethyl-triphenylphosphonium; Zr–Cl), in which the rigid inorganic framework promotes efficient organic room-temperature phosphorescence (RTP) via the heavy-atom effect, and dynamic switching between RTP and STE emission was later achieved through Te^{4+} doping [21]. However, the PLQY of that system remained limited to 42%, and its luminescence regulation mainly relied on a relatively simple competition mechanism between RTP and a single dopant-related STE channel. Herein, we report the first successful incorporation of Sb^{3+} ions into the $ETPP_2ZrCl_6$ lattice (Sb—Zr—Cl), achieving a notable breakthrough in both luminescence efficiency and functional tunability. Unlike the Te^{4+}-doped counterpart, the introduction of Sb^{3+} reconstructs the excitonic energy landscape by generating two distinct Sb-related emissive states, STE_2 (475 nm) and STE_3 (640 nm), in addition to the intrinsic host STE_1 (which is assigned to the $[ZrCl_6]^{2-}$ centered emissive state and is centered at ~630 nm). Although both Te^{4+} and Sb^{3+} belong to the ns^2 cation family, their roles in luminescence regulation are fundamentally different. Te^{4+} mainly introduces a single dopant-related STE channel, whereas Sb^{3+} can activate multiple Sb-related STE states. This multi-STE mechanism not only boosts the PLQY to 98.6% but also enables excitation-dependent luminescence continuously tunable from warm white to orange-red, thereby supporting multilevel anti-counterfeiting, optical information encryption, and light-storage-related applications within a single lead-free material platform.

2 | Results and Discussion

A series of Sb-doped Zr—Cl samples were successfully synthesized via a co-precipitation method, as outlined in the *Experimental Section*. The crystal structure of Zr—Cl was determined using single-crystal X-ray diffraction (SCXRD), revealing a triclinic crystal system with the $\bar{P}_1$ space group. The lattice parameters are a = 10.2367(3) Å, b = 10.3969(3) Å, c = 10.8729(4) Å, and V = 1016.48(6) $Å^3$, with the corresponding crystallographic data summarized in Table S1. As shown in Figure 1a, each Zr^{4+} ion is coordinated by six Cl^- ions, forming discrete $[ZrCl_6]^{2-}$ octahedra. These octahedral units are periodically separated by bulky $ETPP^+$ organic cations, resulting in a typical zero-dimensional (0D) host-guest structure. Figure 1b and Table S2 present the structural details of the $ETPP^+$ cations and $[ZrCl_6]^{2-}$ octahedra, where variations in the Zr—Cl bond lengths and Cl—Zr—Cl bond angles indicate a slight distortion of the octahedral units. The inter-octahedral Zr—Zr distances exceed 10 Å (Figure S1), suggesting negligible electronic coupling between the inorganic units [21, 27–29]. Furthermore, C—H—Cl hydrogen bonds, with lengths ranging from 2.75 to 3.724 Å (Table S3 and Figure S2), indicate weak interactions at the organic-inorganic interfaces. To verify the structural and chemical composition, powder XRD (PXRD), Fourier-transform infrared (FTIR), X-ray photoelectron spectroscopy (XPS), and energy-dispersive X-ray spectroscopy (EDS) mapping were performed on Sb-doped Zr—Cl. The diffraction peaks of Zr—Cl and Sb—Zr—Cl significantly differ from those of the ETPPCl and $ZrCl_4$ precursors but closely match the simulated pattern, confirming the high crystallinity and phase purity of the as-prepared crystals (Figure S3). Additionally, a reference $ETPP_2SbCl_5$ crystal synthesized under identical conditions crystallizes in the monoclinic system with the $C2/c$ space group, excluding the possibility of $ETPP_2SbCl_5$ impurity phases in the Sb—Zr—Cl samples (Figure S4). Rietveld refinement of the powder XRD (PXRD) pattern for the Sb-doped sample (Figure S3c and Table S4), which provides further structural support that the doped material retains the host-derived framework without obvious impurity phases. FTIR spectra show that the C=C stretching vibrations of the benzene ring and the hybrid

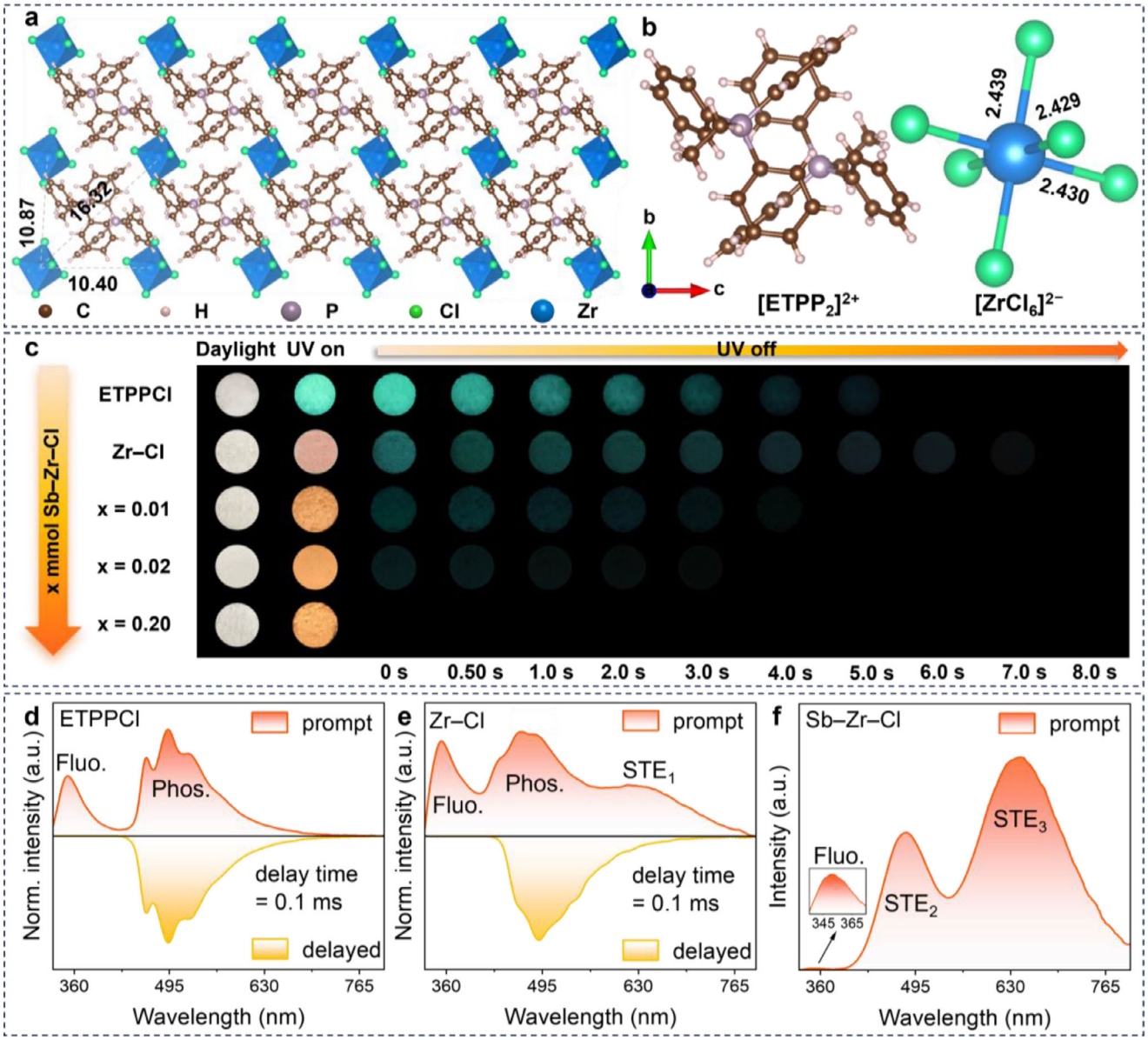

FIGURE 1 | (a) Crystal structure of Zr—Cl (brown: C; pink: H; purple: P; green: Cl; blue: Zr). (b) Molecular structure of $[ETPP_2]^{2+}$ (left) and detailed view of $[ZrCl_6]^{2-}$ octahedron (right). (c) Physics images under daylight and 254 nm excitation of ETPPCl, Zr—Cl, and Sb—Zr—Cl with different Sb^{3+} contents. The prompt and delayed PL spectra of (d) ETPPCl and e) Zr—Cl. Delay time: 0.1 ms. (f) The prompt PL spectrum of Sb—Zr—Cl.

C—H vibration are consistent with those observed for ETPPCl (Figure S5), confirming the structural integrity of the organic groups in Sb—Zr—Cl. XPS analysis reveals the presence of C, P, Zr, Cl, and Sb elements (Figure S6), further verifying the successful incorporation of Sb^{3+} ions. EDS mapping demonstrates homogeneous distributions of P, Zr, Cl, and Sb, with a molar ratio of P:Zr:Cl (24.1:11.6:61.6) (Figure S7), in excellent agreement with the SCXRD result.

Figure 1c presents optical images of ETPPCl, Zr—Cl, and Sb—Zr—Cl crystals under natural light, ultraviolet (UV) irradiation, and after cessation of UV excitation, highlighting their distinct color-responsive behaviors. Under 254 nm illumination, ETPPCl exhibits a cyan-green emission, while the Zr—Cl crystal emits a bright pale-red glow. In contrast, the Sb—Zr—Cl samples all show an orange-red emission. Upon turning off the UV excitation, a visible cyan phosphorescence remains in ETPPCl, Zr—Cl, and trace doped Sb—Zr—Cl crystals, with the Zr—Cl sample displaying the longest-RTP duration up to 7 s (Movie S1). The incorporation of Zr^{4+} not only broadens the emission color range but also significantly extends the phosphorescence lifetime. However, as the nominal $SbCl_3$ feed amount increases, the RTP emission gradually weakens and eventually disappears for the sample prepared with 0.20 mmol $SbCl_3$. This trend is further corroborated by the photophysical characteristics of the $ETPP_2SbCl_5$ crystal (Figure S8). These findings suggest that the synergistic interaction between Zr and Sb plays a key role in regulating both the phosphorescence and fluorescence, endowing the material with promising potential for anti-counterfeiting and information encryption applications.

The photophysical properties of ETPPCl, Zr—Cl, and Sb—Zr—Cl crystals were systematically investigated to elucidate the roles of Zr^{4+} and Sb^{3+} in modulating the luminescence. Both ETPPCl and Zr—Cl exhibit strong deep-UV absorption, and the optical bandgap estimated from the steep high-energy absorption region is around 4.27 eV, consistent with their colorless appearance under ambient light (Figure S9). The weaker low-energy absorption tail above 300 nm, especially the ~333 nm feature in Zr—Cl, is attributed to an intermolecular charge-transfer state [22]. Under 310 nm excitation, the prompt PL spectrum of ETPPCl shows two prominent emission peaks at 360 nm and 490 nm (Figure 1d). Time-resolved PL (TRPL) spectra confirm the dual-emission feature (Figure S10a). High-energy emission (~2.7 ns) originates from organic singlet fluorescence, while low-energy emission (~0.54 s) is due to organic triplet phosphorescence [21, 30, 31]. The delayed PL spectrum shows only a broad low-energy band, which accounts for the visually observable cyan phosphorescence (Figure 1c). The Zr—Cl crystal, incorporating optically inert $[ZrCl_6]$ $[2]^-$ units, exhibits a similar organic emission characteristic, as supported by TRPL analyses (Figures 1e and S10b,c). Additionally, Zr—Cl exhibits an additional broadband emission centered at ~630 nm, with a large Stokes shift of 3.44 eV and a lifetime of 2.7 µs, indicating the presence of a new luminescent center in the system (Figures S10d and S11a). The excitation spectra monitored at different emission wavelengths show a continuous spectral evolution (Figure S11b): as the detection wavelength shifts from the organic-emission region toward the STE-emission region, the organic-related excitation band gradually weakens, while the $[ZrCl_6]^{2-}$-related STE_1 excitation band progressively becomes dominant. This behavior supports the coexistence of two intrinsic emissive channels associated with the organic-related emission and the $[ZrCl_6]^{2-}$-related STE_1 emission, respectively. In addition, the difference between the PLE and overall absorption spectrum is reasonable, because the absorption spectrum reflects all allowed optical transitions in the material, whereas the PLE spectrum is emission-selective and only reflects those excitation pathways that can effectively populate the monitored emissive state. The orange-red emission, characterized by a broad full width at half maxima (FWHM: ~155 nm), a large Stokes shift, and a microsecond-scale lifetime, is consistent with STE_1 emission from $[ZrCl_6]^{2-}$ octahedra, as commonly observed in halide-based systems [21, 32–34]. Notably, Zr—Cl exhibits a prolonged phosphorescence (7 s) compared with ETPPCl (5 s), while its RTP quantum yield (RTPQY) increases from 7.81% to 33.29% (Figure S12). These results suggest that the incorporation of $[ZrCl_6]^{2-}$ enhances the structural rigidity of the $ETPP^+$ framework [21, 26]. For Sb—Zr—Cl, an additional absorption broadband appears in the 310–420 nm region (which is attributed to the Sb^{3+} $^1S_0 \rightarrow {}^3P_{1,2}$ transitions), with its long-wavelength tail extending to about 580 nm, in addition to the intrinsic organic absorption (Figure S13a) [35, 36]. Under 310 nm excitation, dual broadband emissions appear at 475 and 640 nm with lifetimes of 9.4 ns and 4.2 µs, respectively (Figures 1f and S13b). Given their broad profiles, large Stokes shifts, and distinct lifetimes, these emissions are assigned to Sb^{3+}-related STE recombination rather than to organic emissive species. Specifically, the 475 nm emission (STE_2) is assigned to a singlet-derived Sb-centered self-trapped state, for which the radiative transition is spin-allowed and therefore has a characteristically short lifetime in the nanosecond range, whereas the 640 nm emission (STE_3) is assigned to a triplet-derived Sb-centered self-trapped state, whose radiative decay is spin-forbidden and thus exhibits a much longer lifetime on the microsecond timescale [31, 37–40]. This assignment is further supported by the emergence of an additional broadband absorption band at 310–420 nm after Sb doping, which is attributed to the Sb^{3+} $^1S_0 \rightarrow {}^3P_{1,2}$ transitions. Additionally, the parent ETPPCl crystal shows organic fluorescence at ~360 nm and organic phosphorescence at ~490 nm, rather than the newly appeared 475/640 nm dual emission.

To elucidate the origin of the Zr- and Sb-induced STE_1, STE_2, and STE_3 emissions, temperature-dependent prompt PL and PLE spectra of ETPPCl, Zr—Cl, and Sb—Zr—Cl crystals were measured in the temperature range of 80–300 K. As shown in Figure 2a–c and Figure S14, the PL and PLE intensities of three samples gradually decreased with elevation of temperature. For Zr—Cl, excitation-dependent prompt PL spectra further revealed that only STE_1 recombination was observed under <280 nm excitation (Figure S15), confirming the assignment of the high-energy excitation band from intrinsic $[ZrCl_6]^{2-}$. The high-energy excitation band exhibited a progressive blueshift and intensity enhancement during cooling (Figure S14b), which can be attributed to the suppression of electron-phonon coupling within the $[ZrCl_6]^{2-}$ octahedra at low temperatures [11, 14]. Notably, the PLE spectra of Zr—Cl at low-energy region by monitoring 630 nm emission closely resembled those of ETPPCl, especially at elevated temperatures (The dotted rectangle is marked in Figure S14b). Meanwhile, compared with ETPPCl, the ratio of singlet-fluorescence/triplet-phosphorescence in Zr—Cl is significantly smaller (Figure S16). All these results indicate an ET process from the organic single-excited state to STE_1. To validate this ET process, a series of $ETPP_2Zr_{1-x}Sn_xCl_6$ crystals was synthesized, and the evolution of their singlet fluorescence and lifetimes were investigated. With increasing Zr^{4+} content, the organic fluorescence gradually decreases, whereas the $[ZrCl_6]^{2-}$-related STE_1 emission enhances, accompanied by a lifetime decrease from 2.55 to 1.96 ns (Figure S17). These results provide compelling evidence for ET from the organic component to STE_1.

To elucidate the influence of Sb doping on the electron-phonon interaction, the temperature-dependent FWHM of each emission band was fitted individually in Zr—Cl and Sb—Zr—Cl using the Fröhlich longitudinal optical phonon broadening model (Figure S18) [41].

$$\Gamma\ (T) = \Gamma_0 + \Gamma_{LO}/(e^{\eta\omega_{LO}/k_BT} - 1$$

where k_B, Γ_0, Γ_{LO}, and $\eta\omega_{LO}$ represent the Boltzmann constant, temperature-dependent broadening, electron-phonon interaction, and optical phonon energy, respectively. The fitted results show that the values of Γ_{LO} increase from 12.5 ± 0.6 meV (STE_1) to $19.7 \pm 16.7/256.2 \pm 13.2$ meV (STE_2/STE_3), while the values of $\eta\omega_{LO}$ increase from 2.6 ± 0.1 meV (STE_1) to $9.6 \pm 7.6/35.5 \pm 0.2$ meV (STE_2/STE_3) after Sb^{3+}-doping. Although the Γ_{LO} value of STE_3 is relatively large, such a strong effective electron-phonon coupling energy is still physically reasonable for highly self-trapped emissive states with pronounced lattice relaxation. Similar large values have also been reported in related Sb-based low-dimensional halides; for example, the electron-phonon coupling energy of Sb-doped $BTPP_2ZnCl_4$ was reported to be 366 meV [40]. Therefore, the extracted Γ_{LO} values should be regarded as effective fitting parameters and used mainly for comparative analysis. Within this

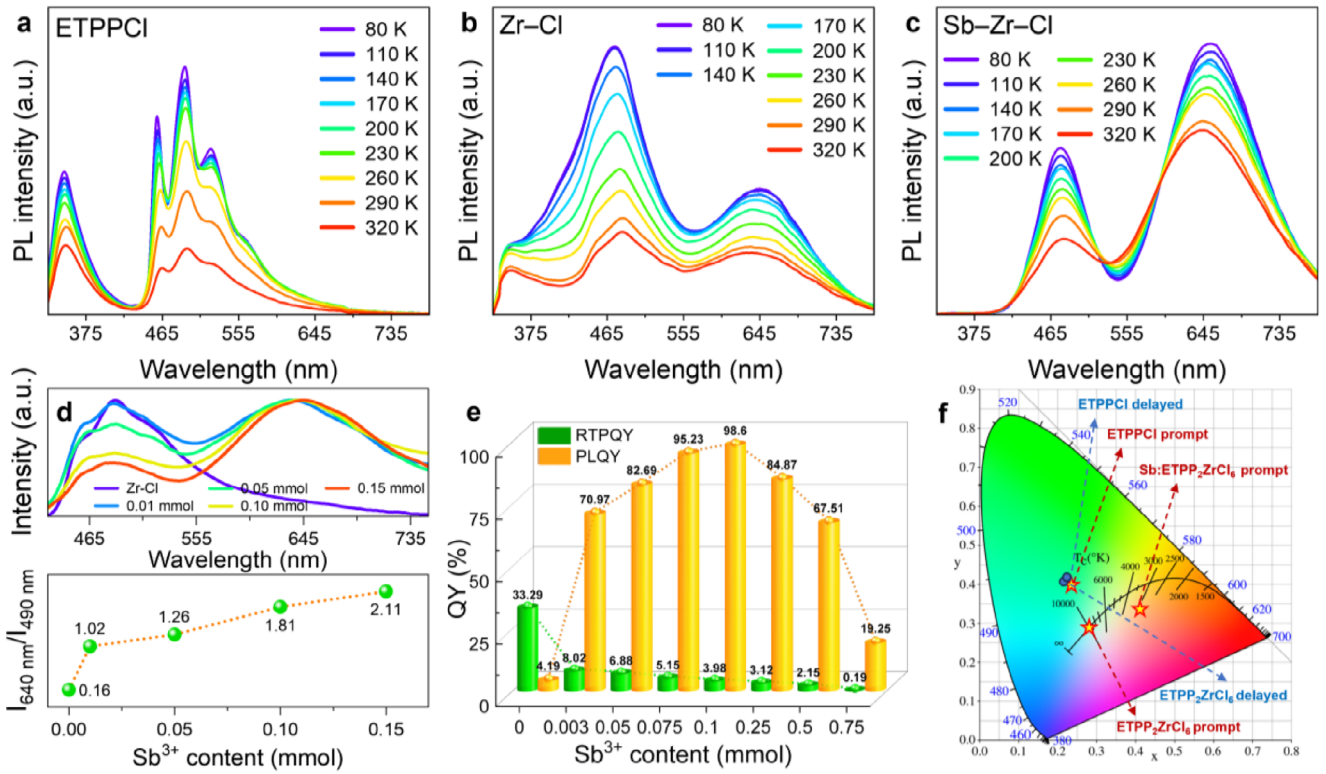

FIGURE 2 | Temperature-dependent prompt PL spectra of (a) ETPPCl, (b) Zr—Cl, and (c) Sb—Zr—Cl. (d) Prompt PL spectra and intensity ratios of 640 to 490 nm for ETPPCl, Zr—Cl, and Sb—Zr—Cl samples prepared with 0.01, 0.05, 0.10, and 0.15 mmol $SbCl_3$ feed amounts, respectively. (e) RTPQYs and PLQYs of, Zr—Cl, and Sb—Zr—Cl with different nominal $SbCl_3$ feed amounts. (f) CIE coordinates of ETPPCl, Zr—Cl, and Sb—Zr—Cl.

framework, the consistently larger Γ_{LO} values for STE_2 and STE_3 than for STE_1 still reliably indicate relatively stronger electron-phonon interaction in the Sb-related emissive centers, which is consistent with their more pronounced self-trapping character. Therefore, the stronger electron-phonon interaction facilitates more carrier localization into the STE_2/STE_3 states, making the PL predominantly governed by Sb^{3+}-related STE emissions [21]. Moreover, the excitation/absorption spectra of Sb—Zr—Cl shows significant overlap with the emission band of the organic component (Figure S19a), indicating that the ET process from the organic excited states to Sb-related states becomes more favorable. Consistent with this interpretation, the phosphorescence and singlet fluorescence lifetimes gradually shorten from 0.66 to 0.13 s and 19.96 to 1.62 ns, respectively, with increasing Sb^{3+} doping concentration (Figure S19b,c). Therefore, Sb-related states provide a more competitive energy-accepting pathway than the original host STE_1 channel. As shown in Figure 2d, time-resolved delayed PL spectra reveal that the RTP intensity gradually decreases with increasing Sb doping content, consistent with the observations presented in Figure 1c. Moreover, the intensity ratio of the 640 nm emission to the 490 nm emission increases from 0.16 to 2.11 with increasing Sb^{3+} concentration, further supporting the enhanced contribution of Sb-related STE emission (Figure 2d). As ET from the organic excited states to the Sb-related self-trapped manifold becomes more efficient, a competitive relationship emerges between Sb-related STE emission and RTP. With increasing Sb^{3+} doping concentration, the RTPQY gradually decreases, whereas the PLQY markedly increases and reaches nearly 100% for the sample prepared with 0.10 mmol $SbCl_3$ (Figure 2e). This optimal value is attributed to the best balance between activation of Sb-related emissive STE channels and the onset of overdoping-induced nonradiative quenching at higher Sb feed amounts. At low nominal $SbCl_3$ feed amounts, the density of Sb-centered emissive states is insufficient to efficiently harvest excitons from the organic component, whereas excessive Sb addition is expected to introduce concentration quenching and additional nonradiative decay pathways. In addition, inductively coupled plasma optical emission spectrometry (ICP-OES) analysis performed on the optimized sample prepared with a nominal $SbCl_3$ addition of 0.10 mmol confirms successful incorporation of Sb, with an actual Sb content of 2.28% (Table S5). The CIE chromaticity coordinates of these materials clearly illustrate their unique luminescence characteristics (Figure 2f).

To further elucidate the origin of the luminescence evolution induced by Sb^{3+} doping, first-principles calculations were performed for Zr—Cl and Sb—Zr—Cl. As shown in Figure 3a, pristine Zr—Cl exhibits an almost flat and discrete band structure with a bandgap of 3.64 eV, indicative of weak intermolecular coupling in this low-dimensional system [40]. The projected density of states (PDOS) analysis reveals that the valence band maximum (VBM) is mainly composed of Cl-p and C-p orbitals, whereas the conduction band minimum (CBM) is primarily derived from the C-p orbitals of the organic ligands together with Zr-d orbitals (Figure 3c). After Sb^{3+} incorporation, hybridization between Sb-s and Cl-p orbitals generates a new antibonding state above the original VBM (Figure 3b), thereby narrowing the bandgap to 2.10 eV. The newly formed VBM is dominated by Cl-p and Sb-s characters, while Sb-p states emerge near the conduction-band edge above the Zr-d states (Figure 3d), consistent with the

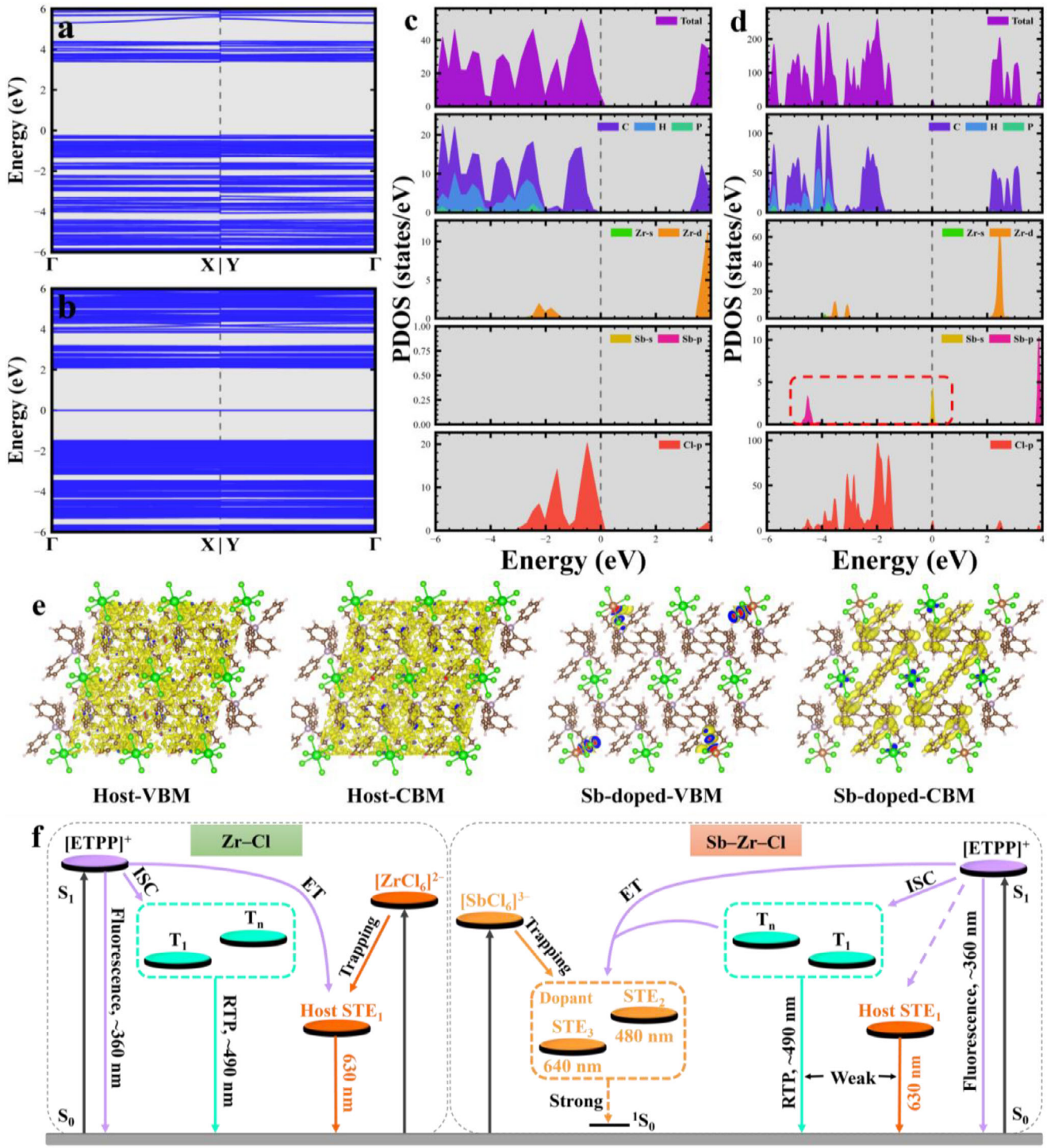

FIGURE 3 | Electronic band structures and corresponding projected density of states (PDOS) of (a,c) Zr—Cl and (b,d) Sb—Zr—Cl, respectively. (e) Charge density isosurface of CBM and VBM for host-related and Sb-doped Zr—Cl. (f) Schematic illustration of the photophysical mechanism in Zr—Cl and Sb—Zr—Cl, highlighting the host-related STE_1 pathway and the Sb-induced self-trapped excited-state composed of STE_2 and STE_3.

experimentally observed absorption in the 310–420 nm region. Moreover, after Sb^{3+} substitutes for Zr^{4+}, the band-edge charge density becomes strongly localized on the Sb atom and its surrounding Cl atoms (Figure 3e), with this localization being particularly pronounced at the valence-band edge. This indicates that photoexcited carriers preferentially localize around the Sb-centered coordination polyhedron, thereby promoting exciton localization and self-trapping, which is consistent with previous reports on related Sb-doped halide systems [39, 42]. Meanwhile, the introduction of Sb dopants also induces slight structural distortion of the inorganic $[ZrCl_6]^{2-}$ octahedra (Figure S20), as reflected by the changes in bond lengths and bond angles relative to the undoped $ETPP_2ZrCl_6$ host (Table S6). These results indicate that Sb doping not only perturbs the local octahedral geometry but also creates a more favorable self-trapping center, which is consistent with the experimentally observed evolution from weak

host-related STE emission to dominant Sb-related STE emission. Therefore, the two Sb-related emissive states are more reasonably assigned to distinct relaxed excited-state branches associated with the Sb-centered excited-state manifold, rather than to different Jahn-Teller distortion modes of the same excited state.

Based on the above discussion, we propose a schematic diagram of the photophysical mechanism as shown in Figure 3f. In Zr—Cl, photoexcitation promotes energy absorption by organic chromophores, driving electrons from the ground state (S_0) to the singlet excited state (S_1). Subsequently, some electrons return to S_0 via radiative transition, generating nanosecond-scale singlet fluorescence, and another fraction enters the triplet state (T_n) through intersystem crossing (ISC) and releases cyan phosphorescence [22, 43, 44]. At the same time, exciton-phonon coupling within the $[ZrCl_6]^{2-}$ unit induces self-trapping and leads to the formation of the host-related STE_1 state. As a result, part of the excitation energy can also be transferred from the organic component to STE_1, giving rise to the host-related STE_1 recombination. For Sb—Zr—Cl, Sb doping reconstructs the excited-state landscape and creates an Sb-related self-trapped excited-state manifold composed of STE_2 and STE_3. Owing to the newly introduced Sb-related absorption channel, the stronger electron-phonon interaction of the Sb-related emissive centers, and the enhanced localization tendency around the Sb-centered cluster, energy transfer from the organic excited states becomes more favorable toward this Sb-related manifold than toward the original host STE_1 pathway. After population enters this Sb-related manifold, redistribution between the higher-energy STE_2 and the lower-energy STE_3 branch gives rise to the experimentally observed dual Sb-related emissions. As a result, the competing RTP pathway is progressively suppressed, while the Sb-related STE emission is markedly enhanced, leading to the observed increase in PLQY.

The as-synthesized crystals exhibit exceptional long-term stability. The material demonstrates exceptional structural and optical stability, as evidenced by the negligible alteration in both its XRD patterns and luminescence spectra after six months of air exposure (Figure S21a,b). The activation energies of the Sb-related emissive states were estimated by fitting the temperature-dependent PL intensity using the following formula (Figure S21c):

$$I(T) = \frac{I_0}{1 + A\exp\left(-\frac{E_a}{k_B T}\right)}$$

where I_0 is the initial PL intensity, A is a fitting constant, k_B is the Boltzmann constant, and T is the temperature. Here, E_a denotes the apparent activation energy associated with thermally activated non-radiative quenching. The obtained values are E_{a2} = 112 meV for STE_2 and E_{a3} = 79 meV for STE_3. Although these values are not exceptionally large in an absolute sense, they are still significantly higher than the thermal energy at room temperature (~26 meV), indicating that thermally activated quenching is effectively suppressed under ambient conditions and supporting the good thermal stability of the STE emission. Furthermore, the emission intensity remains largely unchanged across multiple heating-cooling cycles between 30 and 90°C, confirming its excellent thermal stability and reversibility (Figure S21d). In addition, we further assessed the photostability of Sb—Zr—Cl under continuous UV irradiation. As shown in Figure S21e, the luminescence intensity remains essentially unchanged after prolonged UV excitation, revealing negligible photoinduced degradation. Such excellent photostability, combined with its long-term air stability and thermal stability, highlights the suitability of this material for LED encapsulation and practical optical encryption applications.

Taking advantage of the Sb^{3+}-induced color tunability and the broad lifetime manifold spanning nanosecond fluorescence to second-scale phosphorescence, this material system is particularly well suited for time-gated optical information encryption and anti-counterfeiting. We designed a 4 × 8 dot matrix ASCII (American Standard Code for Information Interchange, Table S7) encoding system based on ETPPCl, Zr—Cl, 0.01 mmol, and 0.20 mmol Sb^{3+}-doped Zr—Cl materials (Figure 4a). In this system, luminescent points are assigned the value "1", while non-luminescent points are assigned the value "0". Under 254 nm excitation, all points emit light, forming a meaningless binary (BIN) code as initial interference information. After the UV light is turned off, time-resolved decoding reveals distinct stages: the pattern decodes to the misleading character "IKUN" at 0.5 s; at 5.00 s, a new BIN code converts to "9882" following decimal (DEC) decoding rules; and by 7.0 s, it further decodes into "0802". Integrating the results from these three time points yield the complete concealed message "IKUN98820802". This multilevel time-sequential encoding strategy based on differences in luminescence lifetimes significantly improves information concealment and encryption strength, making it more difficult to crack without authorization than conventional static fluorescent tag technology, thereby greatly improving information security. As shown in Figure 4b, we also constructed a patterned encoding system. ETPPCl, Zr—Cl, and Sb—Zr—Cl (0.20 mmol Sb) were combined to form a composite pattern in the shape of the number "8888" to verify its multidimensional decoding capability under luminescence responses. The decryption process consisted of three stages: (1) Under natural light, three materials appear colorless, displaying "8888" as the first-layer visual information; (2) Under 254 nm UV excitation, different regions emit distinct fluorescence colors, with pale red emission forming the letter "COOL" as the second encoding layer; and (3) after excitation stopped, the phosphorescent regions exhibit a cyan phosphorescence, transforming the pattern into "0006" as the third-layer hidden information. This three-stage dynamic pattern-decoding design not only reflects the color tunability enabled by Sb doping but also highlights the potential of such materials for multilevel information encryption and high-security anti-counterfeiting. By precisely orchestrating the spatiotemporal response characteristics of fluorescence and phosphorescence, a time-space dual-dimensional information carrier is realized, offering a new approach for developing smart labels and high-security identification technologies.

Sb—Zr—Cl exhibits tunable luminescence ranging from warm white to orange-red under different excitation wavelengths (Figure 5a). As the excitation wavelength shifts from high- to low-energy region, the broadband orange-red gradually intensifies and ultimately dominates the emission. The excitation-dependent emission spectra clearly show dual-band emission

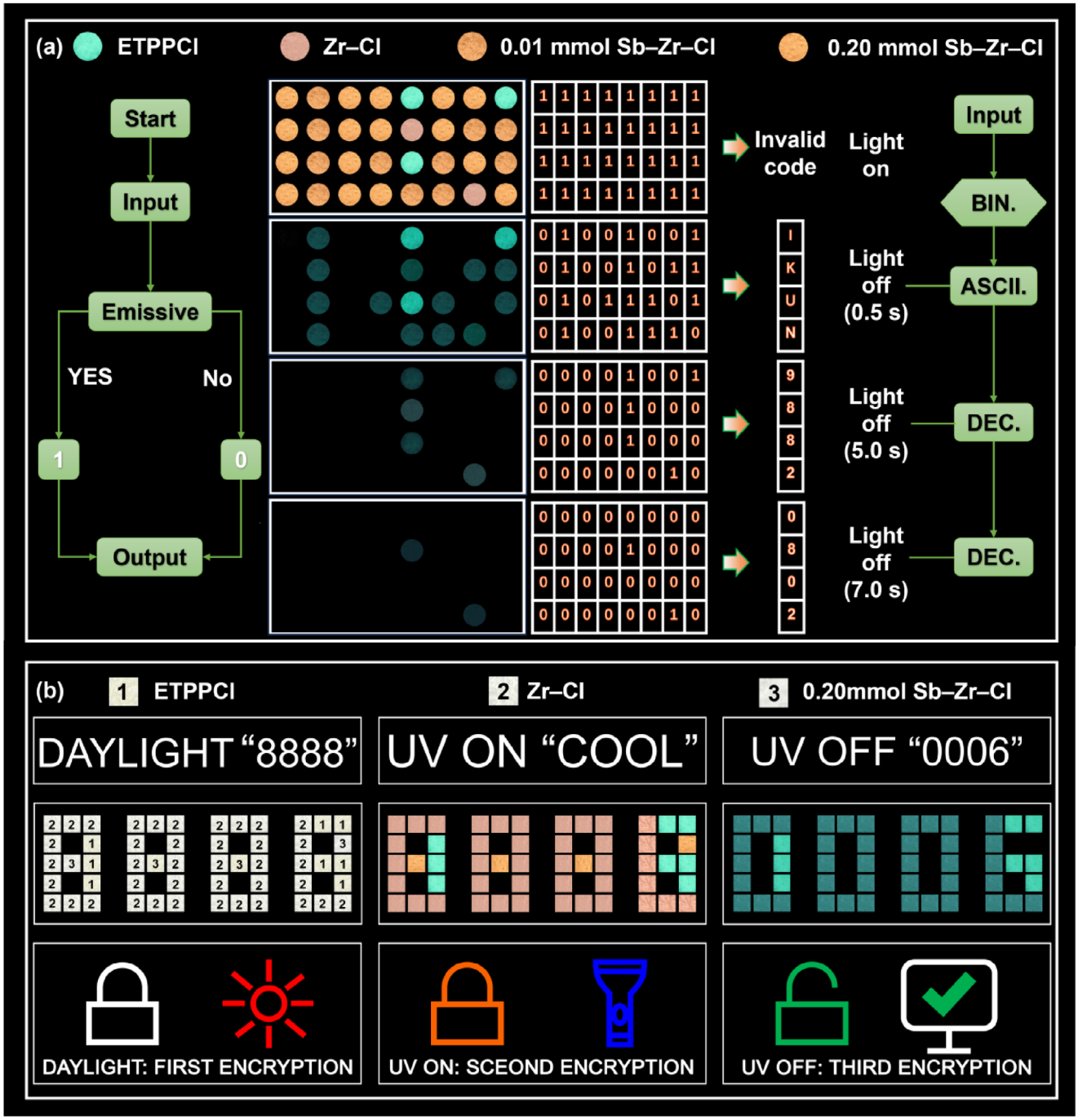

FIGURE 4 | (a) Schematic illustration of the encryption and decryption processes based on the time-resolved anti-counterfeiting. (b) Photographs of the 8888-shaped patterns based on ETPPCl, Zr—Cl and 0.20 mmol Sb—Zr—Cl under daylight, 254 nm UV on, and UV off.

under high-energy excitation (300–360 nm), whereas only the orange-red emission band is observed under longer-wavelength excitation (>360 nm; Figure 5b and Figure S22). This evolution can be quantified by the significant increase in the $I_{640\ nm}/I_{490\ nm}$ ratio with a red-shifting excitation wavelength (Figure 5c), which is further corroborated by the corresponding shift in the CIE coordinates (Figure 5d). Notably, such a pronounced dual-band to single-band redistribution is observed only after Sb incorporation, providing further support that the long-wavelength emission in Sb—Zr—Cl belongs to the Sb-induced STE_3 emission rather than to the original host STE_1 alone. In fact, accurate modulation of the excitation wavelength enables a dynamic redistribution of populations between these two independent STE states, thereby facilitating tunable luminescence [32, 38]. This accounts for the observation of only a single broad emission band under lower-energy excitation. To evaluate whether the high efficiency is maintained under different excitation wavelengths, the PLQY of the optimized Sb—Zr—Cl sample was further measured over an excitation range of 280–370 nm (Figure S23). The results show that PLQY remains above 90% even at longer excitation wavelengths and is maintained at ~98% in the main excitation range of 310–325 nm. These results indicate that the near-unity lumines-

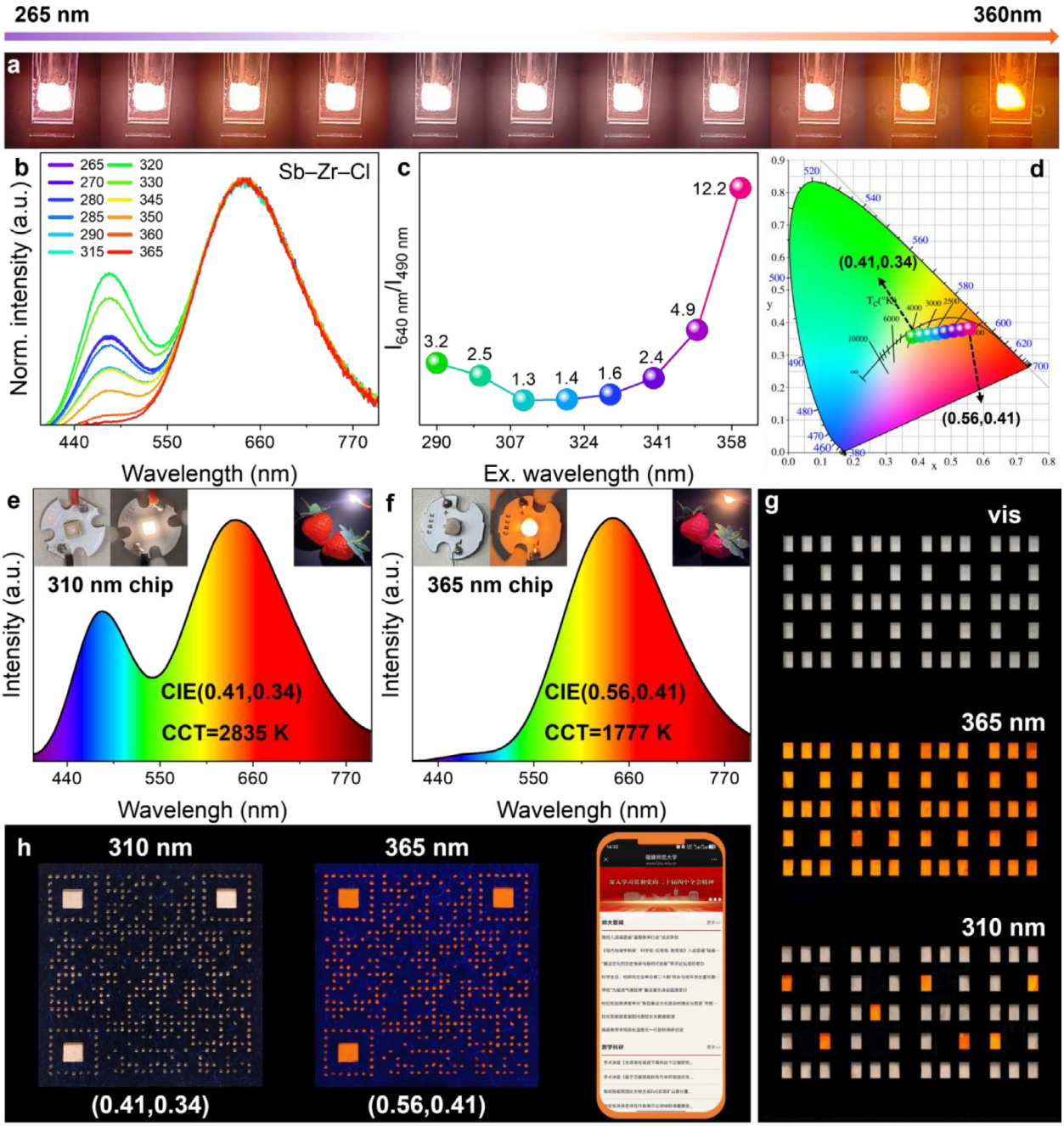

FIGURE 5 | (a) Photographs of Sb—Zr—Cl under UV illumination of different wavelengths. (b) Normalized prompt PL spectra of Sb—Zr—Cl under different excitations. (c) Excitation-dependent prompt PL intensity ratio of $I_{640\ nm}/I_{490\ nm}$ for Sb—Zr—Cl. (d) CIE coordinates of Sb—Zr—Cl. (e,f) Emission spectra of LEDs fabricated by integrating commercial 310/365 nm chips with Sb—Zr—Cl. Inset: Photograph of the working LEDs and strawberry under LED irradiation. Demonstration of practical applications in (g) anti-counterfeiting and (h) information encryption.

cence efficiency is well preserved across the excitation window relevant to the observed excitation-tunable emission. Owing to this distinctive excitation-dependent emission, Sb—Zr—Cl demonstrates potential for applications in solid-state lighting, optical information encryption, and anti-counterfeiting. By integrating commercial UV chips with Sb—Zr—Cl phosphors, color-tunable light-emitting diodes (LEDs) were successfully fabricated. As shown in Figure 5e,f and Figure S24, the LED device with a 310 nm chip emits warm white light with CIE coordinates of (0.41, 0.34) and a correlated color temperature (CCT) of 2835 K, while the device equipped with a 365 nm chip produces orange-red emission with CIE coordinates of (0.56, 0.41) and a CCT of 1777 K. To further demonstrate its capability in information encryption, we constructed a digital display model composed of Sb—Zr—Cl and $Sr_{0.85}Ca_{0.15}AlSiN_3:Eu^{3+}$. Under visible light or 365 nm UV light, the pattern appears as a deceptive message "8888", while under 310 nm excitation, it reveals the true information "2025" through white emission (Figure 5g). Furthermore, the quick response code coated with Sb—Zr—Cl phosphors display distinctly readable white and orange-red fluorescence under different excitation wavelengths. These signals are readily captured by common detection devices and have and have already

been exploited for patterned display on the official website of Fujian Normal University (Figure 5h).

3 | Conclusion

Here, we report a series of Sb—Zr—Cl hybrid metal halides, demonstrating precise modulation of their structural and photophysical properties. The Zr—Cl host crystal adopts a zero-dimensional structure composed of isolated $[ZrCl_6]^{2-}$ octahedra and bulky $ETPP^+$ cations. Strong exciton-phonon coupling within the inorganic units induces Jahn-Teller distortion, leading to the generation of STE_1 emission, while the organic $ETPP^+$ cations contribute long-lifetime phosphorescence. The incorporation of Sb^{3+} dopants creates two distinct Sb-centered self-trapped states, STE_2 and STE_3, which originate from two different relaxed excited-state branches of the Sb-excited-state manifold and efficiently capture organic triplet excitons via the ET process, thereby suppressing RTP and significantly enhancing the PLQY to nearly 100%. Temperature- and excitation-dependent analyses reveal that this emitting behavior of the Sb—Zr—Cl results from a dynamic competition between organic phosphorescence, Zr-related STE_1, and Sb-related STE_2/STE_3 emissions, enabling precise control over emission color, lifetime, and quantum efficiency. The resulting materials exhibit distinctive excitation-dependent luminescence spanning from warm white to orange red, making them ideal for color-tunable LEDs with excellent chromatic adjustability. Beyond optoelectronic performance, the combination of long-lifetime phosphorescence and excitation-dependent emission facilitates advanced information encryption and anti-counterfeiting functionalities. By leveraging luminescence lifetime-dependent time-sequential decoding and patterned emission control, multilevel dynamic optical encoding was achieved, offering a powerful platform for light storage, intelligent labeling, and high-security authentication.

Acknowledgements

This research was supported by the National Natural Science Foundation of China (Nos. 52572155 and 52272141) and Natural Science Foundation of Fujian Province (Nos. 2024J02014 and 2024J01949).

Conflicts of Interest

The authors declare no conflicts of interest.

Data Availability Statement

The data that support the findings of this study are available from the corresponding author upon reasonable request.

References

1. Z. Yang, J. Yao, L. Xu, W. Fan, and J. Song, "Designer Bright and Fast $CsPbBr_3$ Perovskite Nanocrystal Scintillators For High-Speed X-ray Imaging," *Nature Communications* 15 (2024): 8870, https://doi.org/10.1038/s41467-024-53263-9.

2. X. Zhang, D. Chu, B. Jia, et al., "Heterointerface Design Of Perovskite Single Crystals For High-Performance X-ray Imaging," *Advanced Materials* 36 (2024): 2305513.

3. T. Hettiger, R. Jayabalan, A. Sarkar, et al., "Impact of Ligand-Mediated Inductive Effects on Electrochemical p-Doping of $CsPbBr_3$ Nanocrystals," *ACS Energy Letters* 11 (2026): 567–572, https://doi.org/10.1021/acsenergylett.5c03184.

4. J. Li, X. Qiao, B. He, et al., "Biomass-Derived Functional Additive For Highly Efficient And Stable Lead Halide Perovskite Solar Cells With Built-In Lead Immobilisation," *Energy & Environmental Science* 18 (2025): 5632–5642, https://doi.org/10.1039/D4EE06038E.

5. B. Yuan, Z. Wang, S. Zhang, et al., "Atomically Resolved Edges And Defects In Lead Halide Perovskites," *Nature* 647 (2025): 364–368, https://doi.org/10.1038/s41586-025-09693-6.

6. X. Z. Li, Y. Ye, Y. Cao, et al., "Tin-Halide Perovskites For Light-Emitting Diodes," *Chemical Society Reviews* 54 (2025): 6697–6725, https://doi.org/10.1039/D5CS00340G.

7. J. Feng, N. Chen, H. Min, et al., "Interface-Directed Growth of Tin Perovskite for Efficient Light-Emitting Diodes," *Advanced Materials* 37 (2025): 2503007, https://doi.org/10.1002/adma.202503007.

8. J. Qu, Y. Wang, Z. Li, et al., "Origin of Pressure-Induced Nonlinear Optical Property Enhancement in $CsGeCl_3$ Perovskite: $[GeCl_6]$ Octahedron Distortion and Band Gap Closing," *Journal of the American Chemical Society* 147 (2025): 6717–6726, https://doi.org/10.1021/jacs.4c16182.

9. H. K. D. Le, Y. Zhang, P. Behera, et al., "Room-Temperature Ferroelectric Epitaxial Nanowire Arrays With Photoluminescence," *Nano Letters* 24 (2024): 5189–5196, https://doi.org/10.1021/acs.nanolett.4c00453.

10. Q. Yi, H. Bao, H. Li, Z. Song, T. Lyu, and Z. Wei, "Enhanced Photochromism and Thermochromism in Zirconium Halide Perovskite Through Bismuth Doping and Thermal Recrystallization," *Laser & Photonics Reviews* 19 (2025): 2401964, https://doi.org/10.1002/lpor.202401964.

11. W. Zhang, W. Zheng, L. Li, et al., "Multiphoton-Excited Upconversion Luminescence and Amplified Spontaneous Emission From Te^{4+} -Doped Cs_2 $SnCl_6$ Nanocrystals," *ACS Nano* 19 (2025): 18866–18873, https://doi.org/10.1021/acsnano.5c05992.

12. J. Sun, W. Zheng, P. Huang, et al., "Efficient Near-Infrared Luminescence in Lanthanide-Doped Vacancy-Ordered Double Perovskite Cs_2ZrCl_6 Phosphors via Te^{4+} Sensitization," *Angewandte Chemie* 134 (2022): 202201993.

13. W. Liao, K. Han, Y. Wang, and Z. Xia, "Cs_2HfCl_6:Mo^{4+} as Near-Infrared-Emitting Scintillators for Dual-Mode Collaborative Imaging," *Laser & Photonics Reviews* 19 (2025): 2500311, https://doi.org/10.1002/lpor.202500311.

14. Y. Xin, J. Wang, X. Gao, et al., "Ultrabroadband (Vis-NIR) Emission in Single-Component Perovskite LEDs via Tailored Multi-Exciton Energy Transfer Pathways," *Advanced Materials* 37 (2025): 2501658, https://doi.org/10.1002/adma.202501658.

15. F. Zhang, Y. Zhou, Z. Chen, et al., "Large-Area X-Ray Scintillator Screen Based on Cesium Hafnium Chloride Microcrystals Films With High Sensitivity and Stability," *Laser & Photonics Reviews* 17 (2023): 2200848, https://doi.org/10.1002/lpor.202200848.

16. J. Jiang, J. Zheng, H. Fu, et al., "Scalable and Room-Temperature Preparation of Cs_2HfCl_6 Double Perovskites With Recorded Photoluminescence Efficiency and Robust Stability," *Chemical Engineering Journal* 479 (2024): 147543, https://doi.org/10.1016/j.cej.2023.147543.

17. F. Zhang, Y. Zhou, Z. Chen, et al., "Thermally Activated Delayed Fluorescence Zirconium-Based Perovskites For Large-Area And Ultraflexible X-Ray Scintillator Screens," *Advanced Materials* 34 (2022): 2204801.

18. L. Li, J. Jin, K. Han, Y. Wang, and Z. Xia, "Rational Design And Synthesis Of Narrow-Band Emitting Eu(II)-Based Hybrid Halides via Alkyl Thermal Cleavage," *Nature Communications* 16 (2025): 7479, https://doi.org/10.1038/s41467-025-62748-0.

19. L. Han, M. Yuan, H. Xie, et al., "Organic Cation Modulation in Hybrid Zirconium Halides for High-Performance Flexible X-Ray Imaging," *Angewandte Chemie International Edition* 64 (2025): 202425385, https://doi.org/10.1002/anie.202425385.

20. J. Luo, J. Y. Wang, C. M. Shi, L. J. Xu, and Z. N. Chen, "Organic Tellurium (IV) Halide Hybrid as an Efficient Phosphor for Hybrid Light-

Emitting Diodes," *Advanced Functional Materials* 35 (2025): 2424313, https://doi.org/10.1002/adfm.202424313.

21. G. Zhou, Y. Mao, J. Zhang, et al., "Dynamic Phosphorescence/Fluorescence Switching in Hybrid Metal Halides Toward Time-Resolved Multi-Level Anti-Counterfeiting," *Advanced Functional Materials* 35 (2024): 2413524.

22. Z. Luo, Y. Liu, Y. Liu, et al., "Integrated Afterglow and Self-Trapped Exciton Emissions In Hybrid Metal Halides For Anti-Counterfeiting Applications," *Advanced Materials* 34 (2022): 2200607.

23. Z. L. He, J. B. Luo, J. H. Chen, et al., "A Universal Strategy Toward Two-Component Organic-Inorganic Metal Halide Luminescent Glasses And Glass-Crystal Composites," *Science Advances* 11 (2025): adu1982.

24. B. Li, Y. Wang, Y. Xu, and Z. Xia, "Emerging 0D Hybrid Metal Halide Luminescent Glasses," *Advanced Materials* 37 (2025): 2415483.

25. Z. Zhou, J. Zheng, S. Ruan, et al., "A Transparent Hybrid Metal Halide Glassy Scintillation Screen For High-Resolution Fast Neutron Radiography," *Nature Communications* 16 (2025): 6215, https://doi.org/10.1038/s41467-025-61503-9.

26. J. Jin, Y. Wang, K. Han, and Z. Xia, "Rigid Phase Formation and Sb^{3+} Doping of Tin (IV) Halide Hybrids Toward Photoluminescence Enhancement and Tuning for Anti-Counterfeiting and Information Encryption," *Angewandte Chemie International Edition* 63 (2024): 202408653, https://doi.org/10.1002/anie.202408653.

27. W. Zhang, P. Sui, W. Zheng, et al., "Pseudo-2D Layered Organic-Inorganic Manganese Bromide With A Near-Unity Photoluminescence Quantum Yield For White Light-Emitting Diode and X-ray Scintillator," *Angewandte Chemie International Edition* 62 (2023): 202309230.

28. J. Fan, H. Li, W. Liu, and G. Ouyang, "Fabrication Strategies of Mn 2+ -Based Scintillation Screens for X-Ray Detection and Imaging," *Angewandte Chemie International Edition* 64 (2025): 202425661, https://doi.org/10.1002/anie.202425661.

29. W. Zhang, W. Zheng, L. Li, et al., "Unlocking the Potential of Organic-Inorganic Hybrid Manganese Halides for Advanced Optoelectronic Applications," *Advanced Materials* 36 (2024): 2408777, https://doi.org/10.1002/adma.202408777.

30. S. Jin, Q. Huang, L. Wei, et al., "A Thermally Robust Organic–Inorganic Hybrid Scintillator Enabled by RISC-Assisted Mn2+ Emission for High-Temperature X-Ray Imaging," *Laser & Photonics Reviews* 20 (2026): 01917, https://doi.org/10.1002/lpor.202501917.

31. H. Peng, S. Yu, Q. Wei, et al., "Efficient Broadband Near-Infrared Emitters in Lead-Free Metal Halides With Record Photoluminescence Quantum Yield Under Blue Light Excitation," *Advanced Functional Materials* 34 (2024): 2411807, https://doi.org/10.1002/adfm.202411807.

32. H. Peng, X. Kan, W. Huang, et al., "Efficient Tunable White Emission and Blue Light-Excited Near-Infrared Emission in Lead-Free Metal Halide Crystals With Ultra-High Luminous Efficiency for Multispectral Image Fusion and 3D Image Reconstruction," *Advanced Functional Materials* 35 (2025): 2422115, https://doi.org/10.1002/adfm.202422115.

33. Y. Liu, F. Di Stasio, C. Bi, et al., "Near-Infrared Light Emitting Metal Halides: Materials, Mechanisms, and Applications," *Advanced Materials* 36 (2024): 2312482, https://doi.org/10.1002/adma.202312482.

34. D. Liu, P. Dang, G. Zhang, H. Lian, G. Li, and J. Lin, "Near-Infrared Emitting Metal Halide Materials: Luminescence Design And Applications," *InfoMat* 6 (2024): 12542.

35. W. Yang, P. Dang, G. Zhang, et al., "Multimode Luminescence Tailoring in $PMA_4Na(In,Sb)Cl_8$ Organic–inorganic Hybrid Metal Halide via Rigid Benzene Ring Induced Local Lattice Distortion," *Angewandte Chemie International Edition* 63 (2024): 202411136.

36. Z. Wang, D. Xie, F. Zhang, J. Yu, X. Chen, and C. P. Wong, "Controlling Information Duration On Rewritable Luminescent Paper Based On Hybrid Antimony (III) Chloride/Small-Molecule Absorbates," *Science Advances* 6 (2020): abc2181, https://doi.org/10.1126/sciadv.abc2181.

37. Z. Zang, D. Liang, Y. Shi, et al., "Ethanol-Induced Reversible Phase Transition in Antimony Halides for Morse Code Anti-Counterfeiting and Optical Logic Gates," *Laser & Photonics Reviews* 19 (2024): 2401304, https://doi.org/10.1002/lpor.202401304.

38. J. F. Liao, Z. Zhang, L. Zhou, Z. Tang, and G. Xing, "Achieving Near-Unity Red Light Photoluminescence in Antimony Halide Crystals via Polyhedron Regulation," *Angewandte Chemie International Edition* 63 (2024): 202404100, https://doi.org/10.1002/anie.202404100.

39. B. Chen, Y. Guo, Y. Wang, et al., "Multiexcitonic Emission in Zero-Dimensional $Cs_2ZrCl_6:Sb^{3+}$ Perovskite Crystals," *Journal of the American Chemical Society* 143 (2021): 17599–17606, https://doi.org/10.1021/jacs.1c07537.

40. J. Li, K. Liao, J. Zhang, and F. Yuan, "High-Efficiency Ultrabroadband Warm White Light Emission From a Single-Component Lead-Free Perovskite With Record-Low Blue-Violet Content," *Advanced Functional Materials* 36 (2026): 12240, https://doi.org/10.1002/adfm.202512240.

41. S. Jin, H. Yuan, T. Pang, et al., "Boosting STE and Nd^{3+} NIR Luminescence in $Cs_2AgInCl_6$ Double Perovskite via Na^+/Bi^{3+} -Induced Local Structure Engineering," *Advanced Functional Materials* 33 (2023): 2304577, https://doi.org/10.1002/adfm.202304577.

42. F. Zhang, X. Chen, X. Qi, et al., "Regulating the Singlet and Triplet Emission of Sb^{3+} Ions to Achieve Single-Component White-Light Emitter With Record High Color-Rendering Index and Stability," *Nano Letters* 22 (2022): 5046–5054, https://doi.org/10.1021/acs.nanolett.2c00733.

43. D. Guo, W. Wang, K. Zhang, et al., "Visible-Light-Excited Robust Room-Temperature Phosphorescence Of Dimeric Single-Component Luminophores In The Amorphous State," *Nature Communications* 15 (2024): 3598, https://doi.org/10.1038/s41467-024-47937-7.

44. J. Q. Zhao, D. Y. Wang, T. Y. Yan, et al., "Synchronously Improved Multiple Afterglow and Phosphorescence Efficiencies in 0D Hybrid Zinc Halides With Ultrahigh Anti-Water Stabilities," *Angewandte Chemie International Edition* 63 (2024): 202412350, https://doi.org/10.1002/anie.202412350.

Supporting Information

Additional supporting information can be found online in the Supporting Information section.

Supporting File 1: adfm76054-sup-0001-SuppMat.docx.

Supporting File 2: adfm76054-sup-0002-cif.zip.

Supporting File 3: adfm76054-sup-0003-MovieS1.mp4.